PNAS
www.pnas.org

Supplementary Information for

Your main manuscript title

J. Wang, M. Alipour, G. Soligo, A. Roccon, M. De Paoli, F. Picano & and A. Soldati

Alfredo Soldati.
E-mail: alfredo.soldati@tuwien.ac.at

This PDF file includes:

Supplementary text
Figs. S1 to S15 (not allowed for Brief Reports)
Tables S1 to S2 (not allowed for Brief Reports)
Legends for Movies S1 to S5
SI References

Other supplementary materials for this manuscript include the following:

Movies S1 to S5

Supporting Information Text

Methods: Numerical simulations

Numerical simulations are based on an hybrid Eulerian-Lagrangian framework. An Eulerian approach is used to describe the gaseous phase while a Lagrangian approach is used to track the motion of the respiratory droplets. In the following, the numerical framework, the parameters and the initial and boundary conditions adopted for the simulations will be detailed.

Description of the gaseous phase. The velocity, vapor fraction, temperature and density fields of the gaseous phase are described using an Eulerian approach. The governing equations are solved in cylindrical coordinates in an open environment at constant pressure p_0. Considering the larger Reynolds number that characterizes a sneezing event (with respect to a cough), a large eddy simulation (LES) approach is employed. Although the choice of a LES approach may reduce the accuracy of the simulations, a posteriori analysis showed that the results obtained are in excellent agreement with those obtained from direct numerical simulations (DNS). Indeed, for the present configuration and considering the grid resolutions employed for the LES, the regions characterized by high values of the viscous dissipation are extremely localized and their contribution to the overall system dynamics is negligible. Under these hypothesis and after applying the Favre-weighted filtering (1) to the asymptotic low-Mach expansion of the Navier-Stokes system, the governing equations read as follows:

$$\frac{\partial \overline{\rho}}{\partial t} + \frac{\partial \overline{\rho}\tilde{u}_i}{\partial x_i} = \overline{S}_m \, , \qquad [1]$$

$$\frac{\partial \overline{\rho}\tilde{u}_i}{\partial t} + \frac{\partial \overline{\rho}\tilde{u}_i\tilde{u}_j}{\partial x_j} = -\frac{\partial \overline{p}}{\partial x_i} + \frac{\partial}{\partial x_j}\left[(\mu_g + \mu_{sgs})\left(\frac{\partial \tilde{u}_i}{\partial x_j} + \frac{\partial \tilde{u}_j}{\partial x_i} - \frac{2}{3}\frac{\partial \tilde{u}_i}{\partial x_i}\delta_{ij}\right)\right] + (\overline{\rho} - \rho_g)g_i + \overline{S}_{p,i} \, , \qquad [2]$$

$$\frac{\partial \overline{\rho}\tilde{Y}_v}{\partial t} + \frac{\partial \overline{\rho}\tilde{Y}_v\tilde{u}_i}{\partial x_i} = \frac{\partial}{\partial x_i}\left(\overline{\rho}(D + D_{sgs})\frac{\partial \tilde{Y}_v}{\partial x_i}\right) + \overline{S}_m \, , \qquad [3]$$

$$\frac{\partial \tilde{u}_i}{\partial x_i} = \frac{\gamma - 1}{\gamma}\frac{1}{p_0}\left[\frac{\partial}{\partial x_i}\left((k_g + k_{sgs})\frac{\partial \tilde{T}}{\partial x_i}\right) + \overline{S}_e - L_v\overline{S}_m\right] \, , \qquad [4]$$

$$\tilde{T} = \frac{p_0}{\overline{\rho}R_g} \, , \qquad [5]$$

where $\overline{\rho}$, $\tilde{u}_i$, $\tilde{Y}_v$, $\tilde{T}$, $\overline{p}$ are the density, velocity, vapor mass fraction, temperature and hydrodynamic pressure fields while μ_g is the dynamic viscosity of the gaseous phase, D the binary mass diffusion coefficient, k_g the thermal conductivity of the vapor-air mixture and L_v the latent heat of vaporization of the liquid phase. The gaseous phase is assumed to be governed by the equation of state where $R_g = R/W_g$ is the gas constant of the mixture being W_g its molar mass and R the universal gas constant. The ratio $\gamma = c_{p,g}/c_{v,g}$ is the specific heat ratio of the carrier mixture where $c_{p,g}$ and $c_{v,g}$ the gaseous phase specific heat capacity at constant pressure and volume, respectively. In the Navier-Stokes equations, the relative buoyancy force of the jet is accounted via the term $(\overline{\rho} - \rho_g)g_i$ being ρ_g the density of the ambient humid air and g_i the i-th component of the gravity acceleration. The subgrid-scale terms of the Navier-Stokes equations are described using the classical Smagorinsky model (2):

$$\mu_{sgs} = \overline{\rho}(C_s\Delta)^2\left\|\frac{1}{2}\left(\frac{\partial \tilde{u}_i}{\partial x_j} + \frac{\partial \tilde{u}_j}{\partial x_i}\right)\right\| \, , \qquad [6]$$

where C_s is a model constant (0.12 in our setup) and $\Delta = [(r\Delta_\theta)\Delta_r\Delta_z]^{1/3}$ is the typical cell size. For the other subgrid-scale fluxes, D_{sgs} and k_{sgs}, we adopt the gradient model (3) and their value are assumed proportional to the Smagorinsky eddy-viscosity with a constant turbulent Schmidt and Prandtl numbers equal to $Sc_t = 0.66$ and $Pr_t = 0.78$, respectively.

The effects of the dispersed phase on the gaseous phase are accounted for by three sink-source terms, $\overline{S}_m$, $\overline{S}_{p,i}$ and $\overline{S}_e$:

$$\overline{S}_m = -\sum_{k=1}^{n_d}\frac{dm_k}{dt}\delta(x_i - x_{k,i}) \, , \qquad [7]$$

$$\overline{S}_{p,i} = -\sum_{k=1}^{n_d}\frac{d}{dt}(m_k u_{k,i})\delta(x_i - x_{k,i}) \, , \qquad [8]$$

$$\overline{S}_e = -\sum_{k=1}^{n_d}\frac{d}{dt}(m_k c_l T_k)\delta(x_i - x_{k,i}) \, , \qquad [9]$$

where $x_{k,i}$, m_k and T_k are k-th droplet position, mass, velocity and temperature while c_l is the liquid specific heat. The sum is taken over the entire domain droplet population (being n_d the total number of droplets) and, the delta function expresses that the sink-source terms act only at the domain locations occupied by the droplets. These terms are calculated in correspondence of each grid node by volume averaging the mass, momentum, and energy sources from all droplets located within the cell volume centered around the considered grid point.

Description of the respiratory droplets. The motion of the respiratory droplets is described using a Lagrangian approach. In particular, considering the small size of the droplets, these are treated as small rigid evaporating spheres and are approximated as point-wise particles. In addition, the temperature of the liquid phase is assumed to be uniform inside each droplet. As the volume (and mass) fraction of the fluid phase in real coughs and sneezes is relatively small (4–6), the mutual interactions among droplets (i.e collisions, coalescence of droplets) can be neglected. Besides, the effect of the subgrid-scale terms is not taken into consideration. Hence, only the resolved part of the Eulerian fields is used in the equations of the dispersed phase. With these assumptions, the position, velocity, mass and temperature of the droplets are described by the following equations:

$$\frac{dx_{k,i}}{dt} = u_{k,i}\,, \tag{10}$$

$$\frac{du_{k,i}}{dt} = \frac{(\tilde{u}_i - u_{k,i})}{\tau_k}(1 + 0.15 Re_k^{0.687}) + (1 - \frac{\overline{\rho}}{\rho_l})g_i\,, \tag{11}$$

$$\frac{dr_k^2}{dt} = -\frac{\mu_g}{\rho_l}\frac{Sh}{Sc}\ln(1 + B_m)\,, \tag{12}$$

$$\frac{dT_k}{dt} = \frac{1}{3\tau_k}\left[\frac{Nu}{Pr}\frac{c_{p,g}}{c_l}(\tilde{T} - T_k) - \frac{Sh}{Sc}\frac{L_v}{c_l}\ln(1 + B_m)\right]\,, \tag{13}$$

where $x_{k,i}$, $u_{k,i}$, r_k and T_k are the position, velocity, radius and temperature of the k-th droplet while ρ_l is the liquid droplet density, $c_{p,g}$ the specific heat capacity of the gaseous phase at constant pressure and L_v the latent heat of vaporization. The droplet relaxation time, τ_k, and the droplet Reynolds number, Re_k, are defined as:

$$\tau_k = \frac{2\rho_l r_k^2}{9\mu_g}\,, \qquad Re_k = \frac{2\rho_l \|\tilde{u}_i - u_{k,i}\| r_k}{\mu_g}\,, \tag{14}$$

while the Schmidt number, Sc, and Prandtl number, Pr, are computed as:

$$Sc = \frac{\mu_g}{\rho_g D}\,, \qquad Pr = \frac{\mu_g c_{p,g}}{k_g}\,, \tag{15}$$

where μ_g and ρ_g are the dynamic viscosity and density of the gaseous phase while D is the binary mass diffusion coefficient and k_g the thermal conductivity. The Sherwood number, Sh, and Nusselt number, Nu, are estimated as a function of the droplet Reynolds number using the Frössling correlations (7):

$$Sh_0 = 2 + 0.552 Re_k^{1/2} Sc^{1/3}\,, \qquad Nu_0 = 2 + 0.552 Re_k^{1/2} Pr^{1/3}\,. \tag{16}$$

The resulting Sherwood and Nusselt numbers are corrected to account for the Stefan flow (8, 9):

$$Sh = 2 + \frac{Sh_0 - 2}{F_m}\,, \qquad Nu = 2 + \frac{Nu_0 - 2}{F_t}\,. \tag{17}$$

The coefficients F_m and F_t are computed as follows:

$$F_m = \frac{(1 + B_m)^{0.7}}{B_m} H_m\,, \qquad F_t = \frac{(1 + B_t)^{0.7}}{B_t} H_t, \tag{18}$$

where H_m and H_t are defined as:

$$H_m = \ln(1 + B_m)\,, \qquad H_t = \ln(1 + B_t)\,, \tag{19}$$

being B_m and B_t the Spalding mass and heat transfer numbers:

$$B_m = \frac{Y_{v,s} - \tilde{Y_v}}{1 - Y_{v,s}}\,, \qquad B_t = \frac{c_{p,v}}{L_v}(\tilde{T} - T_k)\,, \tag{20}$$

where $\tilde{Y_v}$ and $\tilde{T}$ are the vapor mass fraction and temperature fields evaluated at the droplet position, $Y_{v,s}$ is the vapor mass fraction evaluated at droplet surface and $c_{p,v}$ is the vapor specific heat at constant pressure. The vapor mass fraction at the droplet surface corresponds to the mass fraction of the vapor in a saturated vapor-gas mixture at the droplet temperature. To estimate $Y_{v,s}$, we use the Clausius-Clapeyron relation to first compute the vapor molar fraction, $\mathcal{X}_{v,s}$:

$$\mathcal{X}_{v,s} = \frac{p_{ref}}{p_0}\exp\left[\frac{L_v}{R_v}\left(\frac{1}{T_{ref}} - \frac{1}{T_k}\right)\right]\,, \tag{21}$$

where p_{ref} and T_{ref} are arbitrary reference pressure and temperature and $R_v = R/W_l$ is the vapor gas constant. The saturated vapor mass fraction is then computed using the relation:

$$Y_{v,s} = \frac{\mathcal{X}_{v,s}}{\mathcal{X}_{v,s} + (1 - \mathcal{X}_{v,s})\frac{W_g}{W_l}}\,, \tag{22}$$

where W_g and W_l are are the molar mass of the gaseous and liquid phases.

Numerical method. The numerical code consists of two different modules: i) an Eulerian module that solves the governing equations for the gaseous phase (density, velocity, vapor mass fraction and temperature); ii) a Lagrangian module that solves the equations governing the droplet dynamics (position, velocity, mass and temperature). In particular, the governing equations of the gaseous phase are discretized in space using a second-order central finite differences scheme and they are time advanced using a low-storage third-order Runge-Kutta scheme. Likewise, the governing equations of the droplets are time integrated using the same Runge-Kutta scheme, and a second-order accurate polynomial interpolation is used to evaluate the Eulerian quantities at the droplet position. Please refer to previous works (9–11) for additional validations and tests of the numerical method.

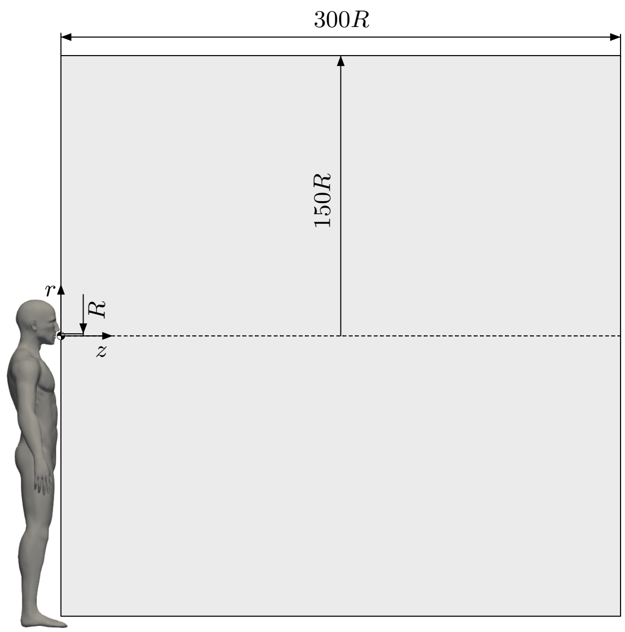

Fig. S1. Sketch of the simulation setup used for the simulations. The computational domain is a cylinder having dimensions $L_\theta \times L_r \times L_z = 2\pi \times 150R \times 300R$ being $R = 1\ cm$ the radius of the circular orifice that mimics the mouth opening. The sneezing jet, together with the respiratory droplets, are injected from the left side of the domain (through the orifice). The domain is initially quiescent (zero velocity) and characterized by a uniform value of temperature, humidity.

Simulation setup. The computational domain, figure S1, is a cylinder into which the droplet-laden sneezing jet is injected through a circular orifice of radius $R = 1\ cm$ located at the centre of the left base that mimics the average mouth opening for females and males subjects (4, 12). The cylinder dimensions are $L_\theta \times L_r \times L_z = 2\pi \times 150R \times 300R$ along the azimuthal (θ) radial (r) and axial (z) directions. The domain is discretized using a staggered grid with $N_\theta \times N_r \times N_z = 96 \times 223 \times 1024$ grid points. The calibration of the numerical parameters (e.g. domain size, grid resolution) is based on previous works (9, 13). In these works, which rely on a very similar model and setup, numerical results have been benchmarked against analytic and experimental results. In addition, further validation tests (e.g. evaporation of an isolated droplet) have been performed and results obtained compared against analytic solutions.

A total mass of liquid equal to $m_l = 8.08 \times 10^{-6}\ kg$ is ejected together with the sneezing jet; the mass of the ejected gaseous phase is equal to $m_g = 2.00 \times 10^{-3}\ kg$. The resulting mass fraction is equal to $\Phi_m = 4.04 \times 10^{-3}$ while the volume fraction is equal to $\Phi_v = 4.55 \times 10^{-6}$ conforming to previous experimental studies (4–6, 14, 15).

The inflow velocity profile of the sneezing jet (figure S2) is obtained from a gamma-probability-distribution function (16) and a simple conversion from dynamic pressure to velocity is implemented based on Bernoulli's principle. The overall duration of the injection stage (sneezing jet and droplets) is about 0.6 s (16). The sneezing jet is characterized by a temperature of $T_j = 308\ K$ and a relative humidity $RH_j = 90\%$ (4, 17, 18) and its peak velocity is $u_{z,j} = 20\ m/s$ (19, 20). Although the values of these parameters, which define the inlet/injection conditions, can sensitively influence the first stage of the sneezing event, their effect in the latter stages of the simulations is expected to be marginal as the ambient conditions are the dominant factors in the evaporation process. From the temperature and relative humidity of the sneezing jet, the density and vapor mass fraction of the jet are obtained from the revised formula reported in Picard *et al.* (2008)(21). The other thermo-physical and transport properties are estimated from Tsilingiris (2008) (22), see table S2 for details.

Considering now the liquid phase (respiratory droplets), for each droplet injected in the computational domain, its initial diameter is assumed to follow a log-normal distribution with geometric mean equal to 12 μm and geometric standard deviation (GSD) equal to 0.7 (23). Albeit being an important parameter, the droplet size distribution is expected to have a minor influence on the final results in terms of suspension and/or deposition of the respiratory droplets, as also shown by previous works (24), see also the section *Sensitivity of simulations to other physical parameters* for further discussion. The above mentioned distribution is generated using a Gaussian random number generator based on a Ziggurat method (25). The initial velocity of the droplets is obtained through interpolation of the velocity field of the gaseous phase in the inlet region, while the initial temperature of the droplets is set to $T = 308\ K$. To mimic the presence of salt, protein and virus dissolved in the respiratory droplets (26), the droplets have a non-volatile core and thus they cannot completely evaporate. This leads to the formation of the so-called droplet nuclei, i.e. the residual part of the respiratory droplets that does not evaporate. In agreement with previous studies (23, 27–31), we consider that the non-volatile core of each droplet represents the 3% of the droplet volume. In terms of droplets size, this means that a droplet can shrink down to $\simeq 30\%$ of its initial diameter. Due to numerical stability issues (9), all generated droplets with an initial size smaller than a critical radius of $0.65\ \mu m$ will be treated as tracers. Likewise, if a droplet, due to the evaporation, becomes smaller than the critical radius, it will be treated as a tracer.

The ambient is assumed quiescent (i.e. all velocity components are initially set to zero) and is characterized by a uniform value of temperature, humidity and constant thermodynamic pressure. The density of the gaseous phase is obtained from the gas equation of state, while the vapor mass fraction is obtained through the Clausius–Clapeyron relation using the sneezing jet conditions as reference.

We perform a total of 7 simulations: a benchmark simulation used for the comparison with the experiments (case S0 in table S2), four production simulations (cases S1-4 in table S2) and two additional simulations used to test the sensitivity of the results (case S5-6 in table S2). The benchmark case considers mono-dispersed non-evaporating droplets (diameter of $2\ \mu m$) released in a sneezing jet having the same temperature of the ambient: $T = 295\ K$ ($22\ °C$) and humidity: $RH = 50\%$ (TU Wien laboratory conditions). The production simulations investigate the effects of ambient temperature and relative humidity on the evaporation process (main results presented in the manuscript). Indeed, considering the constitutive equations of the evaporation process, these two variables are expected to be the physical parameters with the most important effects on the evaporation/condensation process. These simulations consider four different ambient conditions: two different temperatures, $T = 278\ K$ ($5\ °C$) and $T = 293\ K$ ($20\ °C$), and two relative humidity values, $RH = 50\%$ and $RH = 90\%$. The latter two simulations investigate the sensitivity of the results obtained from simulations S1-4 to two specific parameters: the occurrence of multiple sneezing events and the initial droplet size distribution. Specifically, the first simulation considers a case in which a second sneeze follows two seconds after the initial sneeze, while the second considers a case with a different initial size distribution of the injected droplets, namely a Pareto distribution. For these latter cases, the ambient conditions have been kept fixed to $T = 293\ K$ and $RH = 50\%$.

A detailed summary of the simulation parameters and thermo-physical properties adopted for the different simulations is reported in table S1-S2.

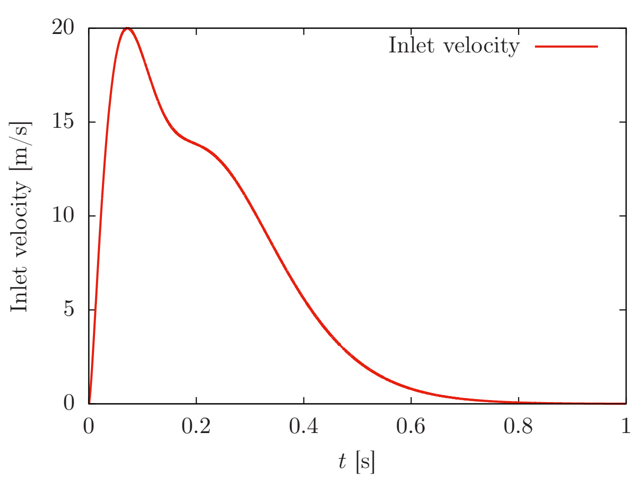

Fig. S2. Inflow velocity of the sneezing jet used in the simulations. The inlet velocity is obtained from a gamma-probability-distribution function (16). The duration of the sneezing event is $\simeq 0.6\ s$ and the peak velocity is $20\ m/s$.

Table S1. Summary of the simulation parameters and thermophysical properties.

Parameter	Symbol	Value	Unit of measurement
Inlet radius	R	1.00 $\times$ 10^{-2}	m
Sneezing jet temperature	T_j	308	K
Sneezing jet relative humidity	RH_j	90$\%$	-
Maximum sneezing jet velocity	$u_{z,j}$	20	m/s
Droplets temperature	T_k	308	K
Mass injected liquid phase	m_l	8.08 $\times$ 10^{-6}	kg
Mass injected gaseous phase	m_g	2.00 $\times$ 10^{-3}	kg
Liquid mass fraction	Φ_m	4.04 $\times$ 10^{-3}	-
Liquid volume fraction	Φ_v	4.55 $\times$ 10^{-6}	-
Environment temperature	T	278 and 293	K
Environment relative humidity	RH	50$\%$ and 90$\%$	-
Environment thermodynamic pressure	p_0	1.01 $\times$ 10^5	Pa
Dynamic viscosity gaseous phase	μ_g	1.99 $\times$ 10^{-5}	Pa s
Thermal conductivity gaseous phase	k_g	2.63 $\times$ 10^{-2}	W/(m*K)
Latent heat of vaporization	L_v	2.41 $\times$ 10^6	J/kg
Universal gas constant	R	2.87$\times$ 10^2	J/(kg*K)
Molar mass of the gaseous phase	W_g	2.89 $\times$ 10^{-2}	kg/mol
Gas constant gaseous phase	R_g	2.92 $\times$ 10^2	J/(kg*K)
Specific heat capacity at constant pressure gaseous phase	$c_{p,g}$	1.03 $\times$ 10^3	J/(kg*K)
Specific heat capacity at constant volume gaseous phase	$c_{v,g}$	7.42 $\times$ 10^2	J/(kg*K)
Specific heat ratio gaseous phase	γ	1.39	-
Vapor specific heat capacity at constant pressure	$c_{p,v}$	1.88 $\times$ 10^3	J/(kg*K)
Vapor phase gas constant	R_v	4.61 $\times$ 10^2	J/(kg*K)
Binary mass diffusion coefficient	D	2.67 $\times$ 10^{-5}	m^2/s
Molar mass liquid phase	W_l	1.80 $\times$10^{-2}	kg/mol
Density liquid phase	ρ_l	1.00 $\times$ 10^3	kg/m^3
Specific heat liquid phase	c_l	4.18 $\times$ 10^3	J/(kg*K)
Volume fraction non-volatile material droplet	Φ_v^c	3$\%$	-
Prandtl number	Pr	0.782	-
Schmidt number	Sc	0.663	-

Table S2. Summary of the main simulation parameters

Case	Temperature	Relative humidity	Density	Vapor mass fraction	Sneezing events	Size distribution
-	T [K]	RH [%]	ρ_g [kg/m^3]	Y_g [	-	-
S0	295	50	1.174	8.22 $\times 10^{-3}$	Single	Monodispersed
S1	278	50	1.245	2.82 $\times 10^{-3}$	Single	Log-normal
S2	278	90	1.245	5.09 $\times 10^{-3}$	Single	Log-normal
S3	293	50	1.181	7.42 $\times 10^{-3}$	Single	Log-normal
S4	293	90	1.181	1.34 $\times 10^{-2}$	Single	Log-normal
S5	293	50	1.181	7.42 $\times 10^{-3}$	Double	Log-normal
S6	293	50	1.181	7.42 $\times 10^{-3}$	Single	Pareto

Methods: Experiments

We set up a laboratory experiment to investigate the dynamics of droplets-laden jets. We used a compressor-based system to supply the flow with air, which is seeded with micrometrical droplets by a liquid seeder. Measurements consist of flow velocity (point wise) and drops distribution (two-dimensional distribution). Details are provided in the following.

Experimental setup. The main components of the system are shown in figure S3(a). To produce repeatable flow conditions, we designed a system in which the flow parameters (pressure, duration) can be carefully controlled. The flow generated by the compressor (pressure 6.5 bar) is controlled by an electromagnetic valve (Parker 4818653D D5L F). The valve is activated by a timer (Finder, relays type 94.02 and plug-in timer 85.02), which is set to maintain the valve open for 0.15 s. We verified *a-posteriori* via hot-wire measurements that the flow is highly repeatable.

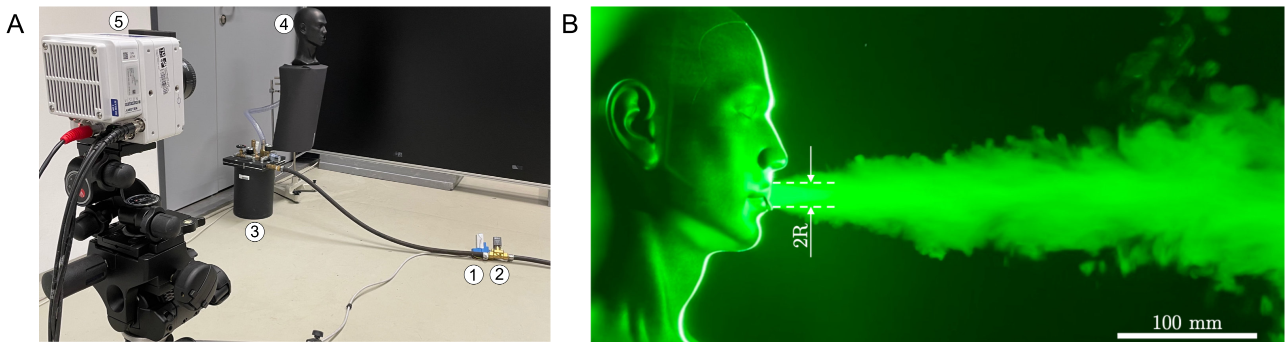

Fig. S3. Panel A shows the experimental setup used. The setup is composed by the compressor (not shown), timer (1), electromagnetic valve (2), liquid seeder (3) and dummy head (4). A laser is used to illuminate the micro-metric droplets. Image acquisition is preformed by a high-speed camera (5). Panel B shows the dummy head used to perform the experiments ($R = 1\ cm$).

The compressor is connected to a seeding generator (9010F0031 Liquid Seeder, type FT700CE), which produces droplet with size falling in the range 1-3 μm, with an average droplets size of 2 μm, as reported in figure S4. To seed the flow with neutrally-buoyant and non-evaporating drops, an aqueous and non-toxic solution (Safex - Inside Nebelfluid, Dantec Dynamics) is used. The solution is kept at the ambient temperature. We observed that the drops remain suspended in the ambient for long time, without any apparent effect of sedimentation. The droplets Stokes number, St, is defined as $St = \rho_l r_l^2 \bar{u}_{z,j}/(R\mu_g)$, being $r_l = 1\ \mu$m averaged droplets radius and $\bar{u}_{z,j} \leq 20$ m/s the reference velocity. For the present case, we obtain $St \leq 0.1$ and we consider the droplets as flow tracers (32).

We used a dummy head to avoid exposure of human beings to the potentially harmful laser light. The droplet-laden jet is emitted through the mouth of the dummy, which is mimicked by a circular opening of radius $R = 1$ cm, see figure S3(B). The mouth is directly connected to the fog generator through a tube of length 100 cm and inner diameter $2R$. The temperature of environment (T), jet (T_j) and droplets (T_k) is constant and equal to $T = T_j = T_k = 295$ K, therefore buoyancy plays no role in the dynamics of the jet, in agreement with the observations of (33). The relative humidity of the air is $RH = 50\%$.

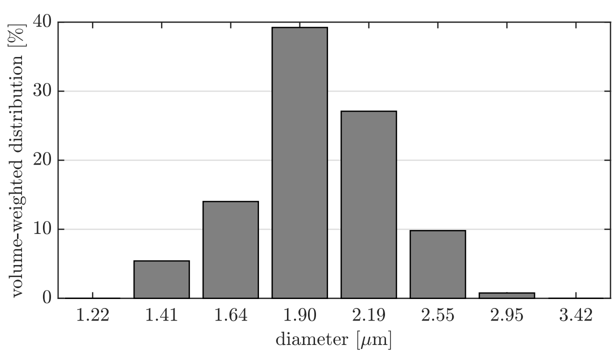

Fig. S4. Volume-weighted droplets distribution [%] as a function of the diameter of the droplets produced (34).

Imaging system. A high-speed laser is used to create a sheet (thickness 4 mm) in which the experimental measurements are performed. The laser consists of a double-pulse laser (Litron LD60-532 PIV, 25 mJ per pulse) illuminating the measurement region at frequency 0.8 kHz. To record the evolution of the flow, we used a Phantom VEO 340L (sensor size of 2560×1600 pixel at 0.8 kHz) equipped with lenses having focal length 35 mm, looking perpendicularly to the laser sheet at a distance of 200 cm. Camera and laser are controlled via a high-speed synchroniser (PTU X, LaVision GmbH, Germany). Images are collected with DAVIS 10 (LaVision GmbH, Germany) and processed in MATLAB to compute the extension of the front of the jet.

As the jet propagates along the axial direction (z), particles concentration reduces. As a result, the light intensity recorded by the cameras drops significantly with z, making the detection of the front of the jet hard to obtain. To perform the edge-detection process, we applied subsequent image processing steps (subtracting background noise, binarization, median filter). After image preprocessing, the boundary of the jet is found by Moore-Neighbor tracing algorithm (35) and finally the edge, the maximum horizontal coordinate of the boundary, is determined and tracked in time. In figure S5 (and as well in the manuscript), the evolution of the front of the jet, L, is reported as a function of time. The mean (red solid line) and standard deviation (error bars) are obtained from 7 independent experiments.

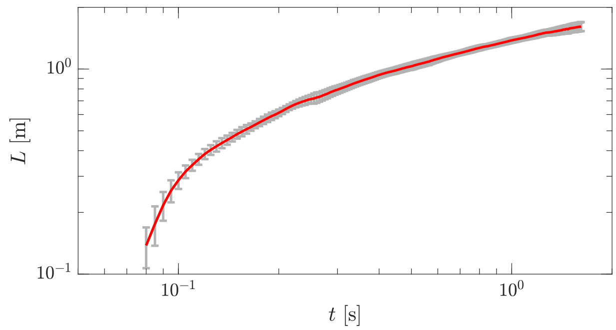

Fig. S5. Evolution of the front of the jet, L, as a function of time, t. Mean (red solid line) and standard deviation (error bars) are obtained from 7 independent experiments. The acquisition rate is 0.8 kHz and we show here one every 4 instants.

Hot-wire anemometry. We used a hot-wire anemometry system (acquisition rate 1 kHz, probe type Dantec 55P11) to measure the axial velocity of the flow and thus to calibrate the inflow velocity profile. Figure S6 shows the axial velocity measured along the centerline of the jet ($r = 0$) at a distance $z = 20$ mm from the mouth as a function of time, t. To characterise the inlet condition, we performed 11 independent experiments. In each experiment, the instantaneous velocity measurements (u_1, grey data) are averaged over a moving window of 20 ms to obtain u_{20} (blue solid line). Then results of all experiments are averaged to obtained the ensemble averaged flow velocity (u, red solid line). The excellent agreement observed between the ensemble average (u) and the single experiment (u_{20}) confirms the repeatability of the flow generated. Finally, the mean value of velocity computed for $0 \leq t \leq 0.7$ s ($\overline{u}$, dashed line) is also shown, and it is used for further comparison with the results obtained from the numerical simulations.

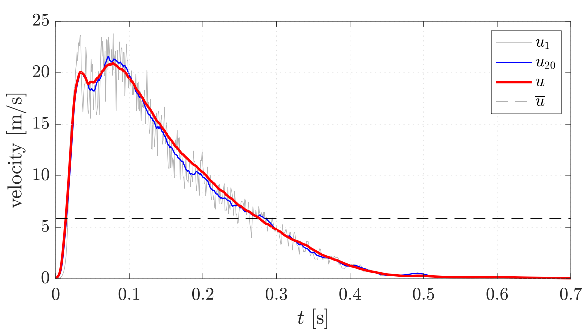

Fig. S6. Time-dependent evolution of the axial velocity measured at the centerline ($r = 0$) at distance $z = 20$ mm from the mouth. Instantaneous velocity measurements (u_1, grey line) as well as the velocity averaged over a moving window of 20 ms (u_{20}, blue line) are shown here for one experiment. Then results of 11 experiments are used to obtained the ensemble averaged flow velocity (u, red solid line). Finally, the mean value computed for $0 \leq t \leq 0.7$ s is shown ($\overline{u}$, dashed line).

Comparison between simulations and experiments

We provide here a quantitative comparison of the experimental and numerical results obtained. The results are analyzed in terms of jet properties in time (distance travelled by the jet) and in space (average jet velocity at different positions). We compute the best-fitting exponent and the corresponding least-squares power-law fit for the two phases of the sneezing event (i.e. jet and puff). Finally, we compare numerical and experimental measurements of the jet velocity at increasing distance from the inlet.

We consider first the initial growth of the jet ($t < 0.6$ s), in which the momentum flux is constant. Indeed, for $t > 0.6$ s the flow-rate at the inlet is negligible, see figure S6. As a result, the expected jet growth obtained using the self-similarity hypothesis (36) is $L \sim t^{1/2}$. Assuming that the initial stage is defined for $0 \leq t \leq 0.6$ s and fitting the results within this time interval, we obtain that the least-squares power-law fits are (with 95% confidence bounds):

- $L(t) = (1.51 \pm 0.03) \times t^{0.51 \pm 0.02}$, with root mean squared error of RMSE $= 0.03$ for the experiments.
- $L(t) = (1.38 \pm 0.04) \times t^{0.51 \pm 0.03}$, with root mean squared error of RMSE $= 0.05$ for the numerical simulations.

The resulting exponents of the power-law scalings obtained numerically and experimentally are in excellent agreement, and match also the theoretical (self-similar) predictions, as shown in figure S7.

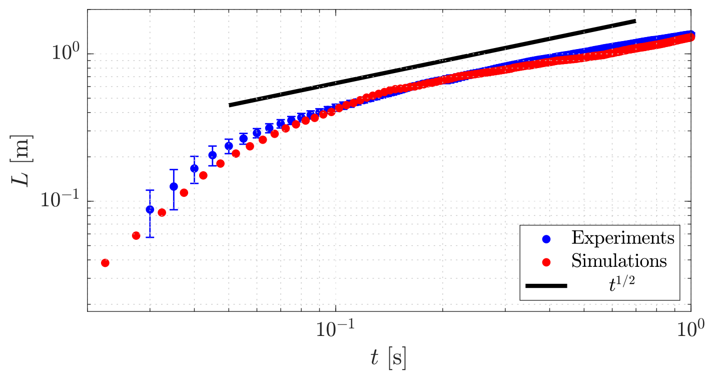

Fig. S7. Distance travelled by the front of the jet in the early-stage of the process (first second of the simulation). Results obtained experimentally (symbols, blue) and numerically (symbols, red) are in excellent agreement with the theoretical (self-similar) predictions ($t^{1/2}$, black solid line).

We consider now the asymptotic scaling exponent ($t > 0.6$ s). During this phase, the flow behaves like a puff and is characterized by constant momentum. The penetration distance, obtained again using the hypothesis of self-similarity (36), evolves as $L \sim t^{1/4}$. Since this phase is longer than the jet phase, we can provide an accurate quantification of the scaling exponent for $t > 0.6$ s. In particular, assuming that $L \sim t^n$, the scaling exponent can be estimated by examining the local slopes, $\frac{d\log(L/R)}{d\log(t/T_0)}$. We use the inlet radius $R = 0.01\ m$ to make the penetration distance dimensionless. Similarly, we use $T_0 = R/u_{z,j}$ to rescale the time, with $u_{z,j} = 20\ m/s$ the maximum sneezing jet velocity. Please note that the quantities used to make the variables dimensionless do not have any effect on the estimate of the scaling exponent. Results of experiments and simulation (symbols) are shown in figure S8 and suggest that, also in this phase, the self-similar solution is attained for long times ($L \sim t^{1/4}$, dashed line).

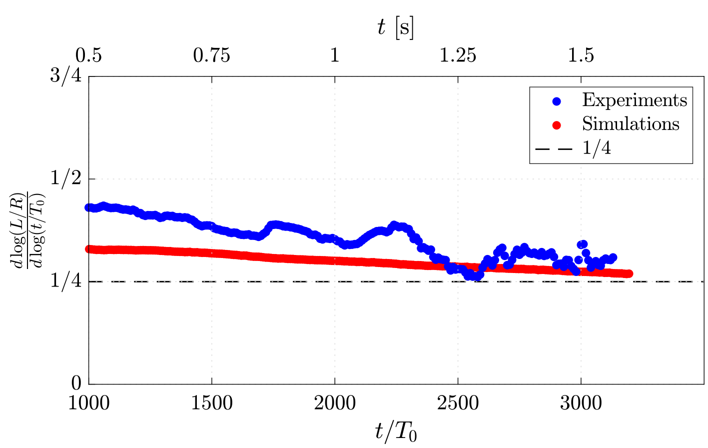

Fig. S8. Evolution in time of the scaling exponent, evaluated by the local slope, $\frac{d\log(L/R)}{d\log(t/T_0)}$ in the late stages of the simulations. We use the inlet radius R to make the penetration distance dimensionless, and $T_0 = R/u_{z,j}$ to rescale the time, being $u_{z,j}$ the maximum sneezing jet velocity. Results of experiments ($0.1\ s$ moving average, blue dots) and simulations (red dots) indicate that, for long times, the self-similar solution ($L \sim t^{1/4}$, dashed line) is attained.

Finally, to further benchmark experimental results against numerical results, we also investigate the evolution of the time-averaged jet velocity, $\overline{u}$, along the axial direction (z axis). The time interval used for the average spans from $t = 0$ s up to $t = 0.6$ s. Concerning the experiments, 76 independent realizations are used to determine $\overline{u}(z)$, which is defined as described above. Measurements are performed along the centerline at 76 equally-spaced z positions. For simulations, data are obtained from the Eulerian grid used to compute the velocity fields and then averaged in time. Results are shown in figure S9 for simulations (red dots) and experiments (blue dots). The velocity profiles are reported normalized by $\overline{u}_0$, i.e. the first velocity value (closest point to the inlet position). The scaling law, $\overline{u} \propto 1/x$, is also reported as a reference (37) with a black, dashed line. As can be appreciated from the figure, experiments and simulations are in excellent agreement over the entire axis span. In addition, both experimental and numerical results well match with the analytic scaling law.

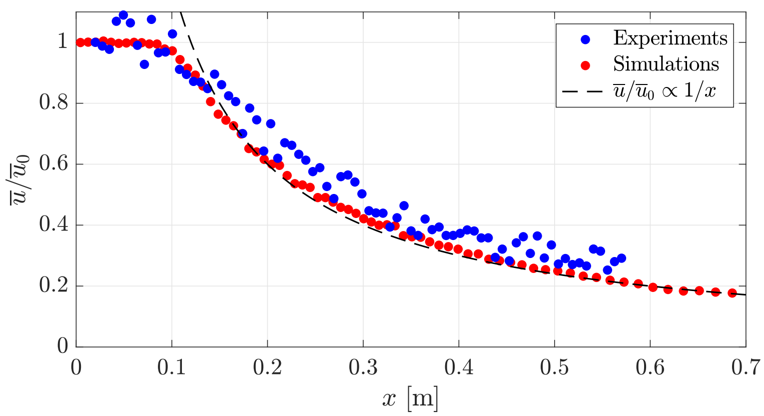

Fig. S9. Time-averaged axial velocity, $\overline{u}$, measured at the jet centerline and normalised by the velocity at the closet point to the inlet position ($\overline{u}_0$), is reported as a function of the distance from the mouth, z. Experimental results are represented using blue dots while simulations results with red dots. As a reference, the scaling law $\overline{u}/\overline{u}_0 \propto 1/x$ (dashed, black line) is also reported.

Sensitivity of simulations to other physical parameters

We present here the results obtained from simulations S5-6. These simulations have been used to assess the sensitivity of the results obtained from simulations S1-4 to two additional factors: the occurrence of multiple sneezing event and the initial droplet size distribution.

Multiple sneezing events. We start by discussing the sensitivity of the results to multiple sneezing events analyzing the results obtained from simulation S5. This simulation considers a second sneeze that occurs two seconds after the initial sneeze. First, we analyze the resulting evaporation times of the droplets, which are shown in figure S10.

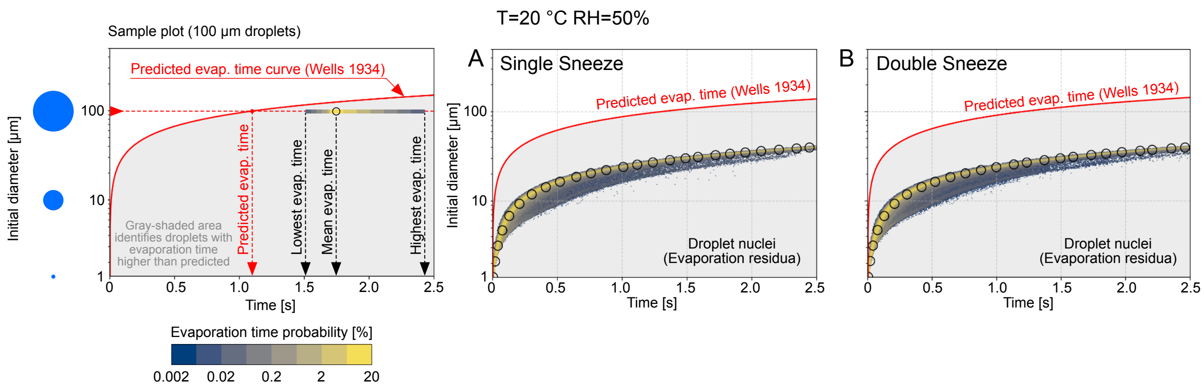

Fig. S10. Distribution of droplets evaporation times for a single sneeze (A) and a double sneeze (B). For any initial diameter, the leftmost side of the distribution indicates the shortest evaporation time, while the rightmost side of the distribution marks the longest evaporation time. Color identifies the probability (blue-low; yellow-high) of having a certain evaporation time. Empty black dots represent the mean evaporation time. The predicted evaporation (d^2-law) is reported with a solid red line.

Panel (A) refers to a single sneeze while panel (B) to a double sneeze. For both cases, the evaporation time is calculated starting from the time at which the droplet is injected in the domain up to the time when the dry nuclei size is reached (i.e. considering the droplet flight time). We observe how the distribution of the evaporation times obtained from the two cases are almost identical. We can thus infer that the first sneeze does not influence the evaporation times of the droplets released during the second sneeze. This behavior can be traced back to the motion of the droplets. Indeed, most droplets are characterized by a small diameter (less than 100 microns) and, as a consequence, their velocity is similar to that of the gaseous phase they are entrained in. Therefore, these droplets are unlikely to sample the conditions of the turbulent gas cloud of moist air released during the first sneeze (located much farther in space and already partially mixed with the ambient air), but instead, they will sample the thermodynamics conditions of the turbulent gas cloud generated by the second sneeze.

Second, we evaluate the dispersion of the droplets analyzing the resulting exposure maps, figure S11.

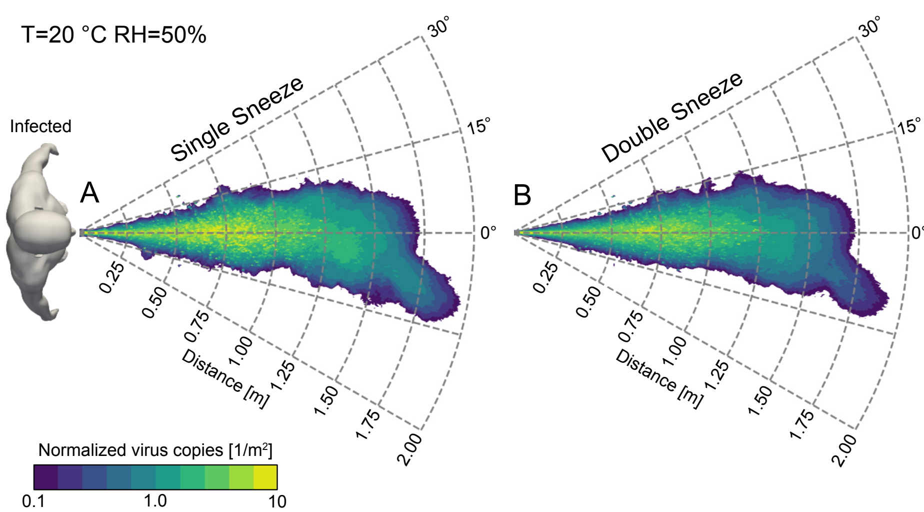

Fig. S11. Virus exposure maps obtained considering a single sneezing event (A) and multiple sneezing events (B). Results are shown normalized by the total number of virus copies ejected during the single sneeze (A) or the two sneezes (B). Results refer to $T = 20°C$ and $RH = 50\%$.

As in the manuscript, exposure maps are computed counting the cumulative number of virus copies that go past a control area in different locations of the domain; data for the exposure maps is collected over a time interval of 4 seconds for both cases. These maps are then normalized dividing by the total number of virions ejected (double for this new case considered). Similar dispersion and spreading in the forward horizontal direction are observed between the single sneeze and the double sneeze case, indicating indeed that the presence on a cloud of warm and moist air emitted during the first sneeze does not particularly affect the evolution of the second sneeze and the dispersion of the droplets emitted. Thus, similarly to the evaporation times, also the virus exposure maps are not significantly influenced by the second sneezing event. Please note that since the results are normalized by the total number of virus copies ejected, for the same value of exposure the dimensional concentration of virus copies is double when a sequence of two sneezes is considered.

Initial droplet size distribution. We move now to discuss the results obtained from simulation S6. This simulation considers the case in which the size of the injected droplets follows a Pareto distribution. We start by analyzing the resulting evaporation times of the droplets, which are reported in figure S12.

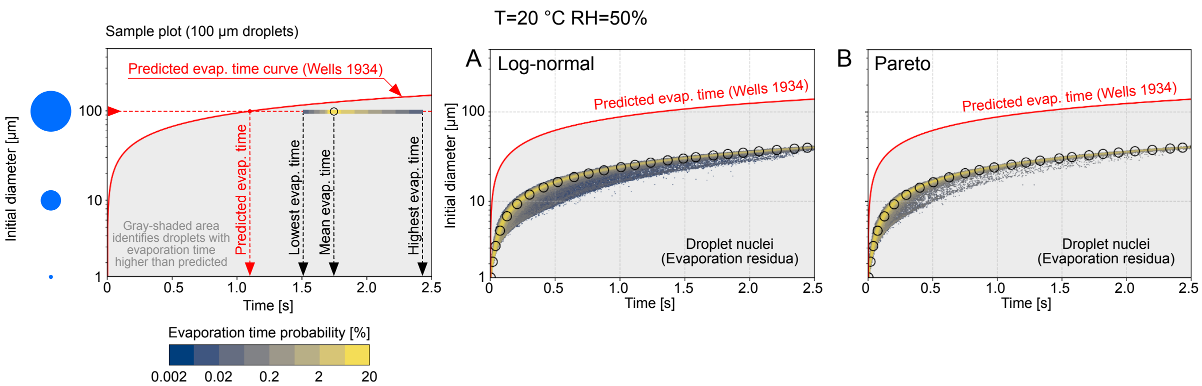

Fig. S12. Distribution of droplets evaporation times when a log-normal (A) and a Pareto (B) distribution are used. For any initial diameter, the leftmost side of the distribution indicates the shortest evaporation time, while the rightmost side of the distribution marks the longest evaporation time. Color identifies the probability (blue-low; yellow-high) of having a certain evaporation time. Empty black dots represent the mean evaporation time. d^2-law predictions are reported with a solid red line.

Looking at the plots, we can observe how the two resulting distributions are very similar. Being the initial size distribution different, marginal difference can be noticed in the number of samples present in the different diameter classes. Overall, this indicates that the evaporation times are not significantly influenced by the prescribed initial size distribution. This behavior can be somehow expected as we are in a dilute regime (low volume fractions).

We move now to the virus exposure maps, which are shown in figure S13.

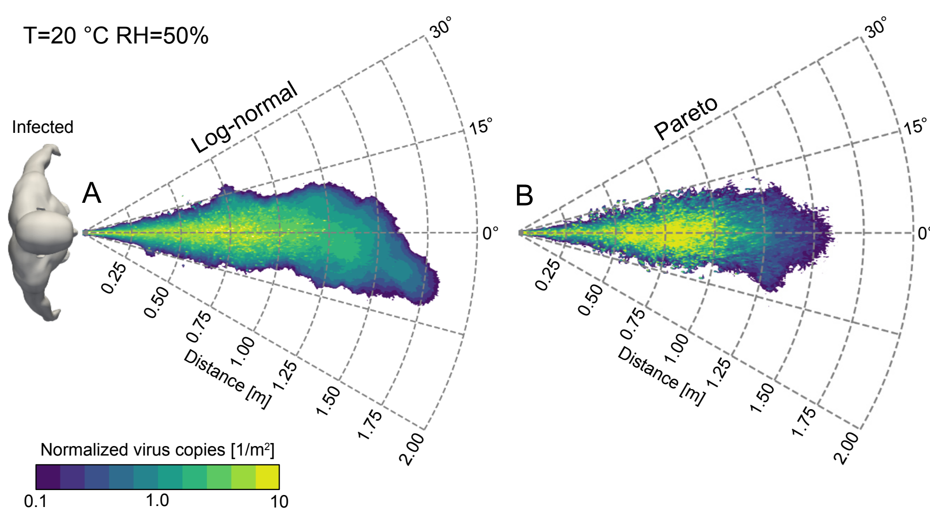

Fig. S13. Virus exposure maps obtained assuming a log-normal distribution (A) and a Pareto distribution (B). Results are shown normalized by the total number of virus copies ejected during the single sneeze (almost the same for both cases). Both simulations consider $T = 20°C$ and $RH = 50\%$.

Panel A refers to the simulation performed using a log-normal distribution (as in the manuscript), while panel B refers to the simulation performed using a Pareto distribution. We can observe that the general picture offered by the exposure map is similar and for both cases there is a core region characterized by a high-level of virus exposure surrounded by an outer region characterized by a lower level of virus exposure. As well, the extension (and thus the dispersion pattern) of the respiratory droplets is similar and for both cases the front of the jet reaches the distance of about 1.65 m. Some differences can be noticed in the transitions between the different levels of virus exposure, which are smoother when a log-normal distribution is used. These difference can be traced back to the lower number of 10 to 15 μm droplets present in the simulation that uses a Pareto distribution. As the liquid mass ejected is the same for both cases, the lack of smaller droplets in the Pareto distribution simulation is balanced out by the presence of larger droplets, which generate hotspots of viral load (and consequently a higher local exposure value), and thus a noisier exposure map.

Effect of face covering

With the aim of briefly discussing the effect of face covering, we performed a series of additional experiments in which different types of protecting devices are adopted. We use advanced imaging techniques to qualitatively evaluate the action of protective devices against droplets spread. In particular, we examine qualitatively the capability of protective devices to prevent the possibility of host-to-host direct contagion. By direct contagion we mean here the exposure to the direct emission of droplets ejected from the mouth or to the droplets carried by the puff propelled forward by the emitter during normal breathing, coughing, sneezing, talking etc. (23). The following configurations have been considered:

- No face-covering device;
- Surgical mask Level I/Type I, conforming to norm ASTM F2100 for US, to EN 14683 for EU and YY-0469 for China (figure S14A);
- Respirator mask N95/FFP2/KN95, conforming to norm NIOSH 42 for US, to EN 149 for EU and GB2626 for China (figure S14B);
- Face shield, conforming to EN 166 for EU (figure S14C).

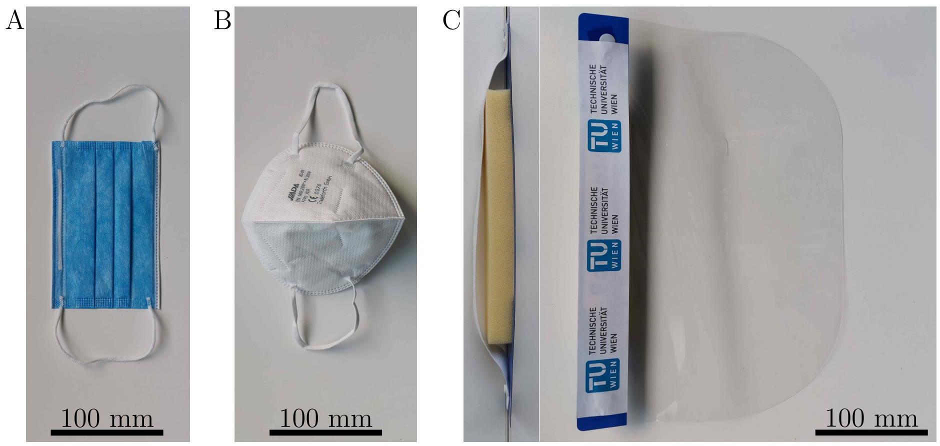

Fig. S14. Face covering devices tested: surgical mask level I/Type I (A), respirator mask N95/FFP2/KN95 (B) and face shield (C, top and front view).

In these experiments, the inlet velocity condition is the same described in figure S6. We show in figure S15 the light intensity distribution recorded using different types of face covering devices. The color indicates the light intensity recorded, from low (white) to high (black) values. The amount of light scattered by the airborne drops and recorded by the cameras is proportional to the local number of drops. Therefore, on a qualitative basis, the light intensity distribution corresponds to the concentration distribution of droplets. The instant considered is the same for all cases shown and corresponds to time $t = 0.15$ s, being $t = 0$ the instant at which the flow starts. One comparative movie (Movie S5) representing the time-dependent evolution of the flow in all configurations considered is also available in the electronic supplementary material. Although these visualizations represent just a qualitative picture of the distribution of droplets emitted, it is possible to analyze the effect of protective devices on the spread of the droplets. We observe in figure S15(B-D) that for all devices considered and in the time window investigated, the advection-diffusion process of the droplets in the horizontal forward direction is decreased with respect to the case without protective devices, shown in figure S15(A). Moreover, we also note that the breathing puffs are mainly evacuated from the venting located at the gaps between the protective devices rims and the face of the dummy. For the face shield, puffs are mainly evacuated downward (i.e. towards the neck of the dummy), whereas for surgical and respiratory masks, a much reduced flow-rate of puffs is evacuated downward/backward towards the neck of the dummy. However, the numbers of droplets emitted from the upper rim (i.e. in the nasal bridge area) is much larger than the number of droplets emitted towards the neck. Eventually the droplets carried by the rising plume are observed to slowly propagate few centimeters in forward direction. From our qualitative analysis, we observe that the action produced by protective devices against droplets spread is effective to prevent host-to-host direct contagion. However, to provide detailed and quantitative information about the impact of the devices on the amount of droplets suspended, further analysis are required. Please also refer to recent works (38, 39) for a detailed discussion on face-covering devices.

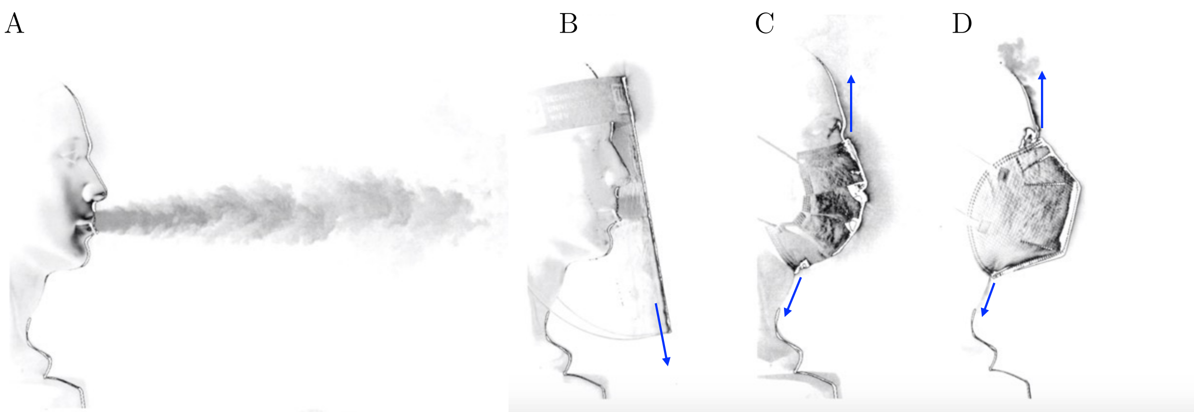

Fig. S15. Comparison of the effect of different type of face covering. "Still" frame taken at $t = 0.15$ s from Movie S5. Experimental measurements are reported in four flow configurations: no face-covering device (A), surgical mask level I/Type I (B), respirator mask N95/FFP2/KN95 (C) and face shield (D). The color indicates the light intensity recorded, from low (white) to high (black) values. On a qualitative basis, the light intensity distribution corresponds to the concentration distribution of droplets. In the configurations considered and in the time window investigated, the advection-diffusion process of the droplets in horizontal forward direction is decreased with respect to the case without protective devices. The breathing puffs are mainly evacuated from the venting occurring at the gaps between the protective devices rims and the face of the dummy.

Movie S1. Movie showing the first 3 seconds of a sneezing event for $T = 5$ °C and $RH = 50\%$. The background shows the local value of the relative humidity (black-low; white-high). The respiratory droplets are displayed rescaled according to their diameter (not in real scale) and are also colored according to their size (red-small; white-large). From the movie, the presence of localized supersaturated regions where $RH > 100\%$ (white) can be appreciated. The upward motion of the sneeze cloud produced by buoyancy and, of part of the respiratory droplets, can be also appreciated.

Movie S2. Movie showing the first 3 seconds of a sneezing event for $T = 5$ °C and $RH = 90\%$. The background shows the local value of the relative humidity (black-low; white-high). The respiratory droplets are displayed rescaled according to their diameter (not in real scale) and are also colored according to their size (red-small; white-large). For this setting (low temperature and high relative humidity), large supersaturated regions ($RH > 100\%$) can be observed. Droplets present in these regions, due to the local humidity conditions, can possibly grow in size (condensation) instead of shrinking.

Movie S3. Movie showing the first 3 seconds of a sneezing event for $T = 20$ °C and $RH = 50\%$. The background shows the local value of the relative humidity (black-low; white-high). The respiratory droplets are displayed rescaled according to their diameter (not in real scale) and are also colored according to their size (red-small; white-large). For this configuration (moderate temperature and low humidity), supersaturated regions are only observed in the beginning of the sneezing event. Nevertheless, most of the droplets are located in regions with a local relative humidity value larger than the ambient. Thus their evaporation dynamics is much slower than predicted by analytic models (e.g. d^2-law).

Movie S4. Movie showing the first 3 seconds of a sneezing event for $T = 20$ °C and $RH = 90\%$. The background shows the local value of the relative humidity (black-low; white-high). The respiratory droplets are displayed rescaled according to their diameter (not in real scale) and are also colored according to their size (red-small; white-large). Also for this setting, the larger temperature (with respect to $T = 5$ °C) limits the extension of the supersaturated regions even though the ambient humidity is close to the saturation value.

Movie S5. Movie showing a comparison of the effect of different type of face covering. The evolution of the flow for $0 \leq t \leq 1s$ of a sneezing event is considered. Experimental measurements are reported in four flow configurations: no face-covering device (A), surgical mask level I/Type I (B), respirator mask N95/FFP2/KN95 (C) and face shield (D). The colour indicates the light intensity recorded, from low (black) to high (white) values. On a qualitative basis, the light intensity distribution corresponds to the concentration distribution of droplets. In the configurations considered and in the time window investigated, the advection-diffusion process of the droplets in horizontal forward direction is considerably decreased with respect to the case without protective devices. The breathing puffs are mainly evacuated from the venting occurring at the gaps between the protective devices rims and the face of the dummy.

References

1. Favre A (1983) Turbulence: Space-time statistical properties and behavior in supersonic flows. *Phys. Fluids* 26(10):2851.
2. Smagorinsky J (1963) General circulation experiments with the primitive equationsi. the basic experiment. *Mon. Wea. Rev.* 91(3):99–164.
3. Schmidt H, Schumann U (1989) Coherent structure of the convective boundary layer derived from large-eddy simulations. *J. Fluid Mech.* 200:511–562.
4. Bourouiba L, Dehandschoewercker E, Bush JW (2014) Violent expiratory events: on coughing and sneezing. *J. Fluid Mech.* 745:537–563.
5. Johnson G, et al. (2011) Modality of human expired aerosol size distributions. *J. Aerosol Sci.* 42(12):839–851.
6. Duguid JP (1946) The size and the duration of air-carriage of respiratory droplets and droplet-nuclei. *J. Hyg.* 44(6):471–479.
7. Froessling N (1968) On the evaporation of falling drops, Technical report.
8. Abramzon B, Sirignano W (1989) Droplet vaporization model for spray combustion calculations. *Int. J. Heat Mass Transf.* 32(9):1605–1618.
9. Dalla Barba F, Picano F (2018) Clustering and entrainment effects on the evaporation of dilute droplets in a turbulent jet. *Phys. Rev. Fluids* 3(3).
10. Picano F, Battista F, Troiani G, Casciola CM (2011) Dynamics of PIV seeding particles in turbulent premixed flames. *Exp. Fluids* 50(1):75–88.
11. Rocco G, Battista F, Picano F, Troiani G, Casciola CM (2015) Curvature effects in turbulent premixed flames of h 2/air: A dns study with reduced chemistry. *Flow Turbul. Combust.* 94(2):359–379.
12. Gupta JK, Lin CH, Chen Q (2009) Flow dynamics and characterization of a cough. *Indoor air* 19(6):517–525.
13. Wang J, Dalla Barba F, Picano F (2021) Direct numerical simulation of an evaporating turbulent diluted jet-spray at moderate reynolds number. *Int. J. Multiph. Flow* 137:103567.

14. Dbouk T, Drikakis D (2020) On coughing and airborne droplet transmission to humans. *Phys. Fluids* 32(5):053310.
15. Dbouk T, Drikakis D (2020) On respiratory droplets and face masks. *Phys. Fluids* 32(6):063303.
16. Busco G, Yang S, Seo J, Hassan Y (2020) Sneezing and asymptomatic virus transmission. *Phys. Fluids* 32(7):073309.
17. Ferron G, Haider B, Kreyling W (1988) Inhalation of salt aerosol particles—i. estimation of the temperature and relative humidity of the air in the human upper airways. *J. Aerosol Sci.* 19(3):343–363.
18. Morawska L, et al. (2009) Size distribution and sites of origin of droplets expelled from the human respiratory tract during expiratory activities. *J. Aerosol Sci.* 40(3):256–269.
19. Xie X, Li Y, Chwang A, Ho P, Seto W (2007) How far droplets can move in indoor environments-revisiting the wells evaporation-falling curve. *Indoor air* 17(3):211–225.
20. Bourouiba L (2020) Turbulent gas clouds and respiratory pathogen emissions: potential implications for reducing transmission of COVID-19. *JAMA* 323(18):1837–1838.
21. Picard A, Davis RS, Gläser M, Fujii K (2008) Revised formula for the density of moist air (cipm-2007). *Metrologia* 45(2):149–155.
22. Tsilingiris P (2008) Thermophysical and transport properties of humid air at temperature range between 0 and 100°c. *Energy Convers. Manag.* 49(5):1098–1110.
23. Balachandar S, Zaleski S, Soldati A, Ahmadi G, Bourouiba L (2020) Host-to-host airborne transmission as a multiphase flow problem for science-based social distance guidelines. *Int. J. Multiph. Flow* p. 103439.
24. Rosti ME, Olivieri S, Cavaiola M, Seminara A, Mazzino A (2020) Fluid dynamics of COVID-19 airborne infection suggests urgent data for a scientific design of social distancing. *Sci. Rep.* 10:22426.
25. Marsaglia G, Tsang W (2000) The ziggurat method for generating random variables. *J. Stat. Softw.* 005(i08).
26. Vejerano EP, Marr LC (2018) Physico-chemical characteristics of evaporating respiratory fluid droplets. *J. R. Soc. Interface* 15(139):20170939.
27. Chaudhuri S, Basu S, Kabi P, Unni VR, Saha A (2020) Modeling the role of respiratory droplets in Covid-19 type pandemics. *Phys. Fluids* 063309:1–12.
28. de Oliveira P, Mesquita L, Gkantonas S, Giusti A, Mastorakos E (2020) Evolution of spray and aerosol from respiratory releases: theoretical estimates for insight on viral transmission. *medRxiv*.
29. Smith SH, et al. (2020) Aerosol persistence in relation to possible transmission of SARS-CoV-2. *Phys. Fluids* 32(10):107108.
30. Redrow J, Mao S, Celik I, Posada JA, Feng Z (2011) Modeling the evaporation and dispersion of airborne sputum droplets expelled from a human cough. *Build. Environ.* 46(10):2042–2051.
31. Stadnytskyi V, Bax CE, Bax A, Anfinrud P (2020) The airborne lifetime of small speech droplets and their potential importance in SARS-CoV-2 transmission. *Proc. Natl. Acad. Sci. USA* 117(22):11875–11877.
32. Tropea C, Yarin AL (2007) *Springer handbook of experimental fluid mechanics.* (Springer Science & Business Media).
33. Yang F, Pahlavan AA, Mendez S, Abkarian M, Stone HA (2020) Towards improved social distancing guidelines: Space and time dependence of virus transmission from speech-driven aerosol transport between two individuals. *Phys. Rev. Fluids* 5(12):122501.
34. Dantec Dynamics (2009) *Seeding Generator for LDA and PIV.*
35. Gonzalez RC, Eddins SL, Woods RE (2004) *Digital image publishing using MATLAB.* (Prentice Hall).
36. Sangras R, Kwon O, Faeth G (2002) Self-preserving properties of unsteady round nonbuoyant turbulent starting jets and puffs in still fluids. *J. Heat Transfer* 124(3):460–469.
37. Xu C, Nielsen PV, Gong G, Liu L, Jensen RL (2015) Measuring the exhaled breath of a manikin and human subjects. *Indoor Air* 25(2):188–197.
38. Cheng Y, et al. (2021) Face masks effectively limit the probability of SARS-CoV-2 transmission. *Science*.
39. Bagheri G, Thiede B, Hejazi B, Schlenczek O, Bodenschatz E (2021) Face-masks save us from SARS-CoV-2 transmission. *arXiv preprint 2106.00375*.